

Supporting information

Exploration of VPO₄ as a new anode material for sodium-ion batteries

Xinghui Liang,^a Xing Ou,^{a,*} Hong Dai,^b Fenghua Zheng,^a Qichang Pan,^a Peipei Liu,^a

Xunhui Xiong,^a Meilin Liu^c and Chenghao Yang,^{a,*}

a. Guangzhou Key Laboratory for Surface Chemistry of Energy Materials, New Energy Research Institute, School of Environment and Energy, South China University of Technology, Guangzhou 510006, P. R. China.

b School of Materials Science and Engineering, Central South University, Changsha, 410083, P.R. China

c School of Materials Science & Engineering, Georgia Institute of Technology, Atlanta, GA30332-0245, USA

E-mail: esouxing@mail.scut.edu.cn, esyangc@scut.edu.cn

Experimental Section

Synthesis of VPO₄@C composite.

Stoichiometric ratio (1:1:0.2:0.5) of vanadium (III) acetylacetonate (C₁₀H₁₄O₅V), ammonium phosphate ((NH₄)₂HPO₄), glucose (C₆H₁₂O₆) and oxalic acid (C₂H₂O₄) were sequentially dissolved in deionized water under continuous stirring and heating. The C₁₀H₁₄O₅V was added as vanadium source and carbon source simultaneously. After forming a sol precursor, then the mixed solution was continuously stirred and heated at 80°C to achieve the gel, followed by drying in a vacuum oven at 100 °C overnight (freeze drying). Finally, the as-prepared powders were obtained by sintering at 300°C for 3 hours and 900°C for 1 hour in Ar/H₂ (95:5) atmosphere.

Material characterizations

X-ray diffraction (XRD) was collected with Bruker Advance D8 diffractometer using Cu K α source. Thermogravimetric analysis (TGA) was carried out by a Mettler Toledo TGA/DSC-1100. Raman test was conducted by a LabRAM Aramis spectrophotometer with a laser wavelength of 532 nm. X-ray photoelectron (XPS) was recorded on a LabRAM Analyzer with wavelength of 514 nm. Scanning electron microscopy (SEM) and Transmission electron microscopy (TEM) were performed on JEOL JSM-7500FA and JEOL-2011 at 200 kV equipped with energy-dispersive X-ray spectroscopy (EDS), respectively.

The *in-situ* XRD measurement was recorded by home-design cell and as reported previously.^{S1,S2} The cell was made of stainless steel and inset with an internal slot with 12-mm diameter, while the configuration was illustrated in Fig.S1. Specifically,

the beryllium foil served as transition window to allow X-ray passage, and the carbon paper acted as a current collector. The electrode was obtained by mixing the active material (VPO_4/C) and polyvinylidene fluoride binder (PVDF) with a ratio of 8:2, which were homogeneously dispersed by the N-methylpyrrolidinone (NMP) solvent and then cast onto the carbon paper. Each XRD pattern was performed in steps of 0.02° and scanned between $2\theta=10^\circ-60^\circ$ at the rate of $0.08^\circ \text{ s}^{-1}$. There was a 30 s interval for each required pattern. The corresponding charge/discharge measurement was carried out at the rate of 100 mA g^{-1} , ensuring that at least 40 scans can be recorded for an entire sodiation/desodiation cycle.

Electrochemical measurements

The as-prepared electrodes were prepared by mixing VPO_4 (70%), carbon black (20%), and PVDF (10%) in NMP solvent. The slurry was coated on copper foil, followed by drying in a vacuum oven. The electrodes were punched into round disks with $1.0-1.2 \text{ mg cm}^{-2}$ loading of active material, and then assembled in the glovebox by sodium metal, glass fiber (Whatman GF/D) and $1.0 \text{ M NaCF}_3\text{SO}_3$ dissolved in diethylene glycol dimethylether (DEGDME) as reference/counter electrode, separator and electrolyte, respectively. The galvanostatic tests were conducted on a Land System (CT2001A) in the potential range of $0.01-3.0 \text{ V}$. Cyclic voltammogram (CV) at a scan rate of 0.1 mV s^{-1} and electrochemical impedance spectroscopy (EIS) measurements over the frequency range from 100 kHz to 0.01 Hz were performed on a CHI660E electrochemical workstation and IM6 (Zahner) electrochemical station, respectively.

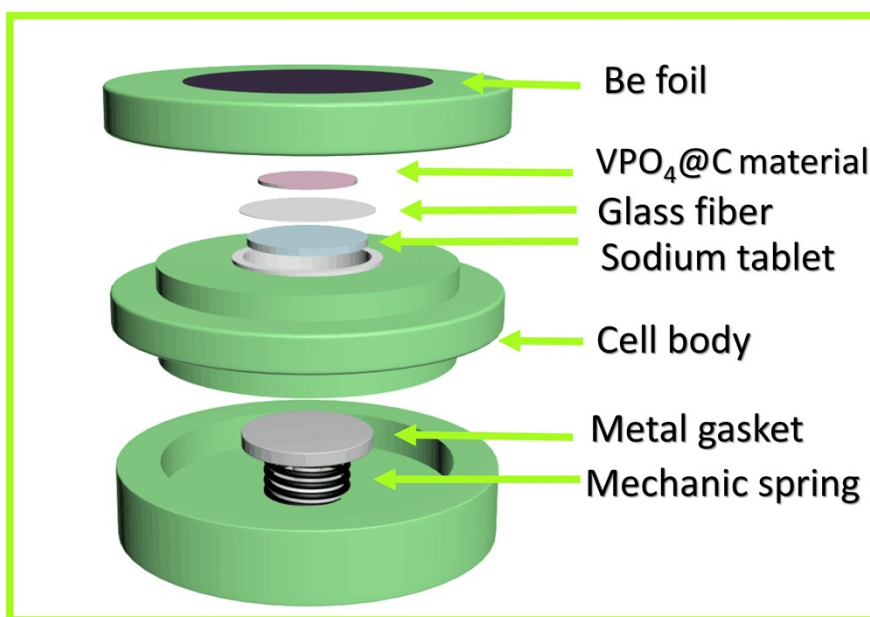


Fig. S1. The configuration of *in-situ* battery cell.

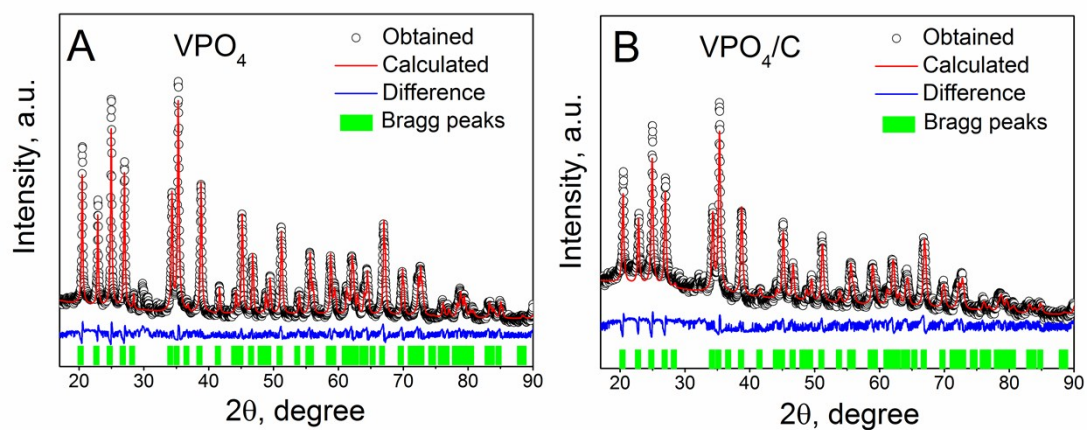


Fig. S2. Rietveld refinement XRD pattern of bare VPO₄ (A) and VPO₄@C (B).

Table S1. Experimental lattice parameters calculated from the Rietveld refinement for bare VPO₄ and VPO₄@C composites.

Samples	a (Å)	b (Å)	c (Å)	V(Å ³)	R _{wp}	R _p
VPO ₄	5.2212093	7.7634015	6.2760865	254.39705	25.67	20.13
VPO ₄ @C	5.2284616	7.7828670	6.2657795	254.96974	20.32	16.59

Table S2. Structural parameters calculated from the Rietveld refinement for bare VPO₄

Atom	site	x	y	z	Occ.
V1	4a	0.00000	0.00000	0.00000	1
P1	4c	0.00000	0.35055	0.25000	1
O1	8g	0.24720	0.47002	0.25000	1
O2	8f	0.00000	0.24518	0.03811	1

Table S3. Structural parameters calculated from the Rietveld refinement for the VPO₄@C

Atom	site	x	y	z	Occ.
V1	4a	0.00000	0.00000	0.00000	1
P1	4c	0.00000	0.35497	0.25000	1
O1	8g	0.24826	0.46801	0.25000	1
O2	8f	0.00000	0.24148	0.04237	1

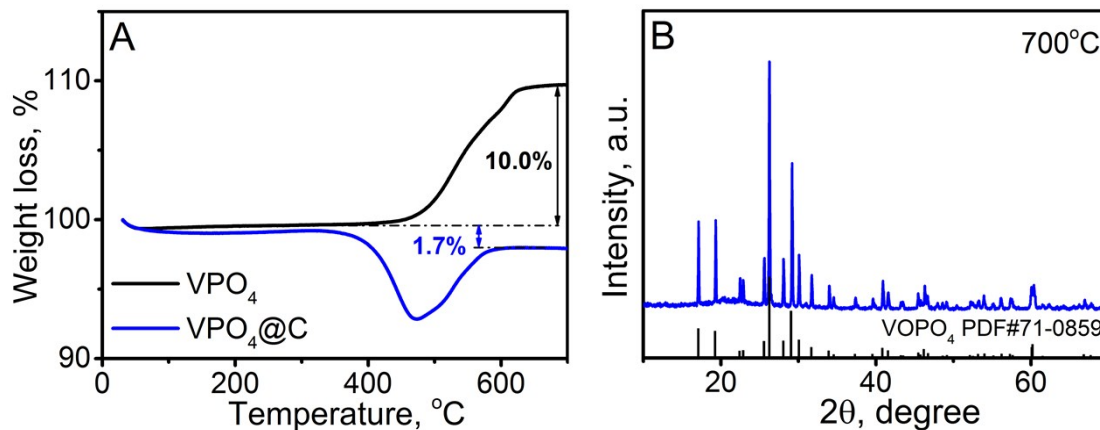


Fig. S3. TGA measurement of bare VPO_4 , and $\text{VPO}_4@\text{C}$ composites in the temperature range of 30-700 °C in the flowing of air atmosphere (A), XRD patterns for final product of VPO_4 sintered at 700 °C under air atmosphere (B).

TGA test is operated in air flow to calculate the carbon content of $\text{VPO}_4@\text{C}$ (Fig. S3A). The apparent increasing mass of bare VPO_4 is corresponded to the oxidation of VPO_4 to VOPO_4 (Fig. S3B). In contrast, the rapid mass loss starting from 400°C for $\text{VPO}_4@\text{C}$ sample is related to the removal of carbonous materials.

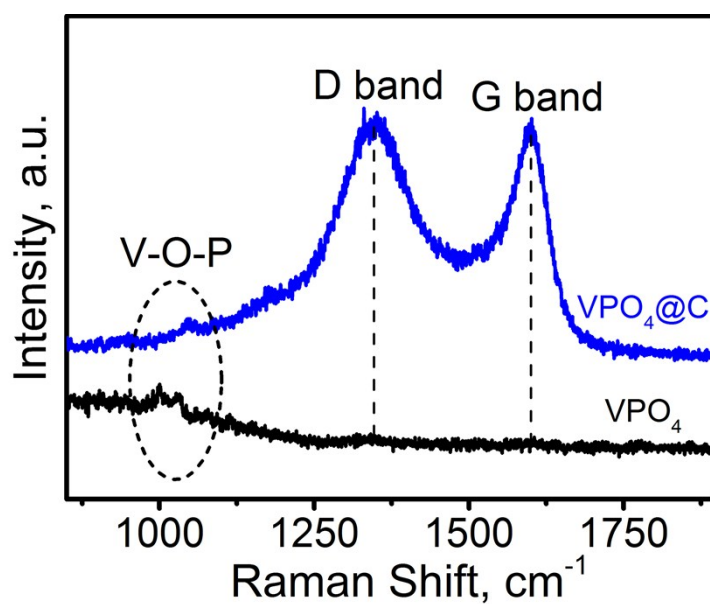


Fig. S4. Raman spectrum of bare VPO_4 and $\text{VPO}_4@\text{C}$ composites.

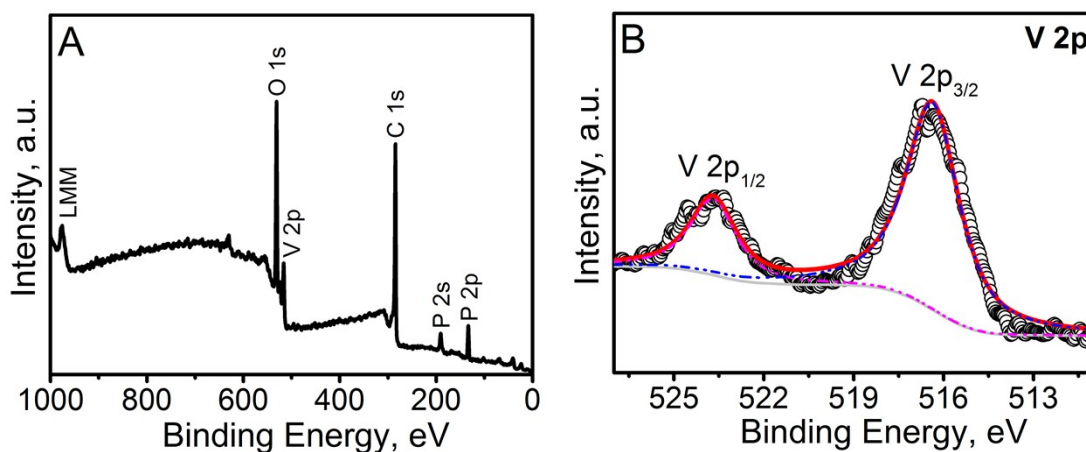


Fig. S5. XPS full pattern (A) and core level of V 2p (B) for $\text{VPO}_4@\text{C}$ composites.

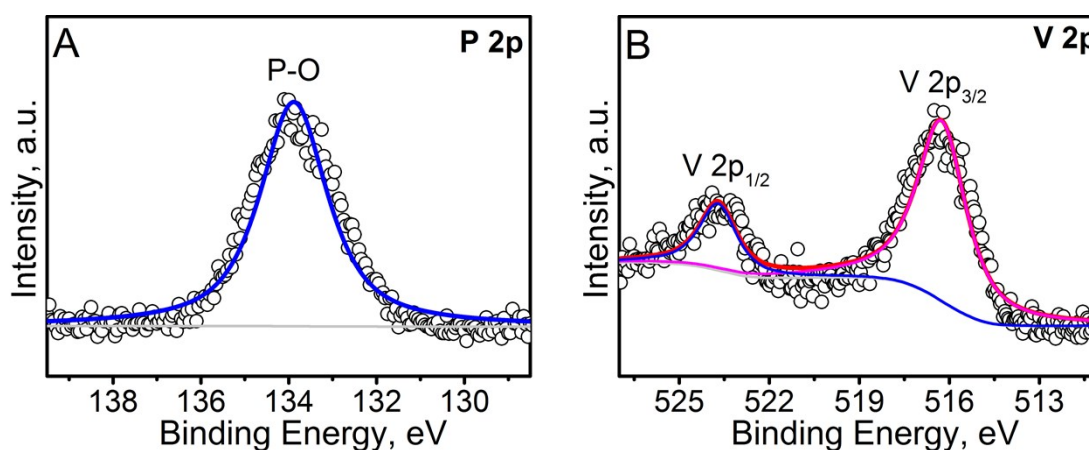


Fig. S6. XPS core level of V 2p (A) and P 2p (B) for bare VPO_4 .

It is clearly observed that the binding energy of P 2p spectrum for bare VPO_4 is 133.9 eV, which is higher than that of $\text{VPO}_4@\text{C}$ composite. The difference of P 2p spectrum between VPO_4 and $\text{VPO}_4@\text{C}$ is ascribed to that the P 2p spectrum of bare VPO_4 can only be fitted into one peak, which is assigned to the P-O bond. The result is consistent with other literatures.^{S3,S4}

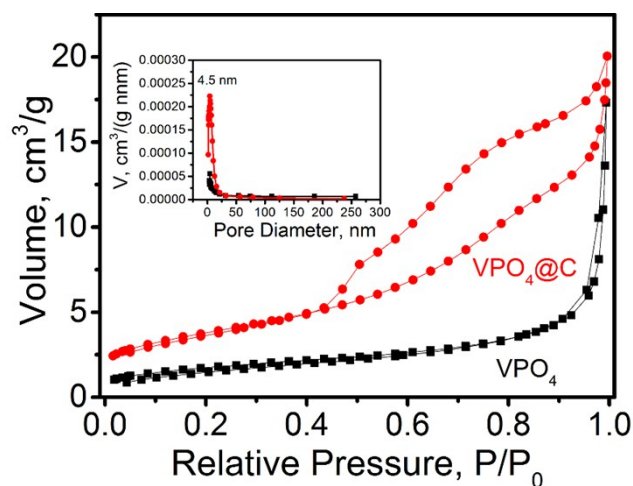


Fig. S7. N₂ adsorption–desorption isotherms and (inset) the pore size distributions of bare VPO₄, and VPO₄@C composite.

According to the Brunauer-Emmett-Teller (BET) measurements, the corresponding specific surface area of the VPO₄@C is 13.51 m² g⁻¹, which is larger than that of VPO₄ (6.22 m² g⁻¹). For VPO₄@C composite, the larger surface area with porous structure is beneficial to Na⁺ transportation and electrolyte diffusion.

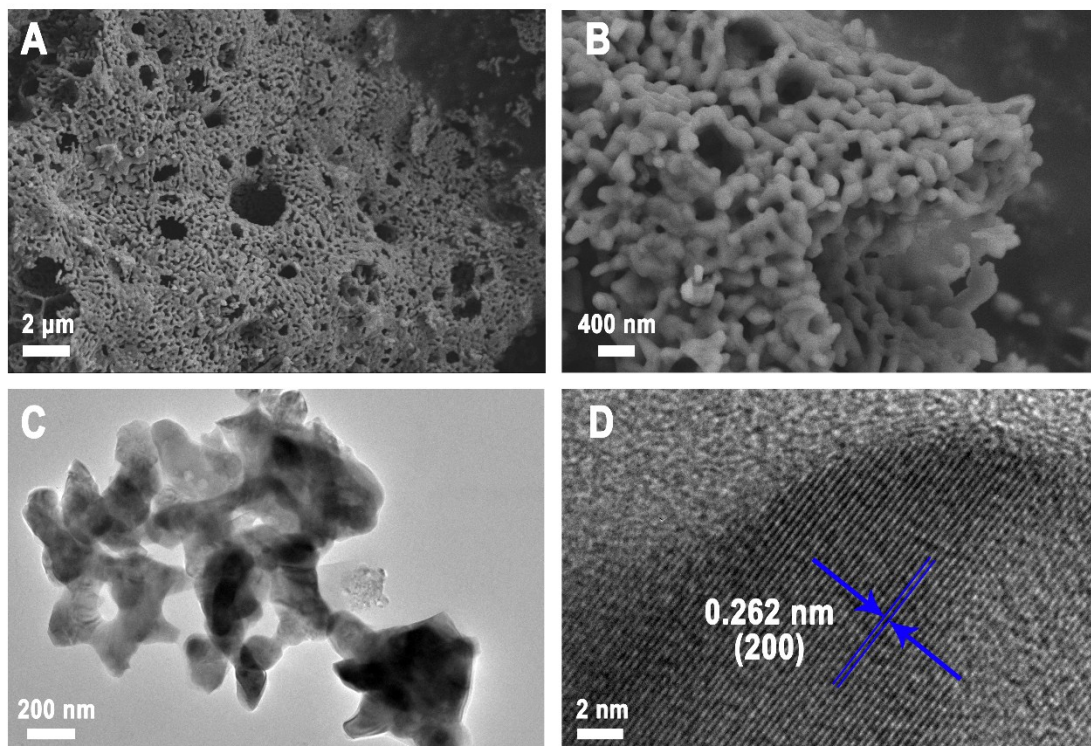


Fig. S8. SEM (A, B), TEM and (C) HRTEM (D) images of VPO_4 .

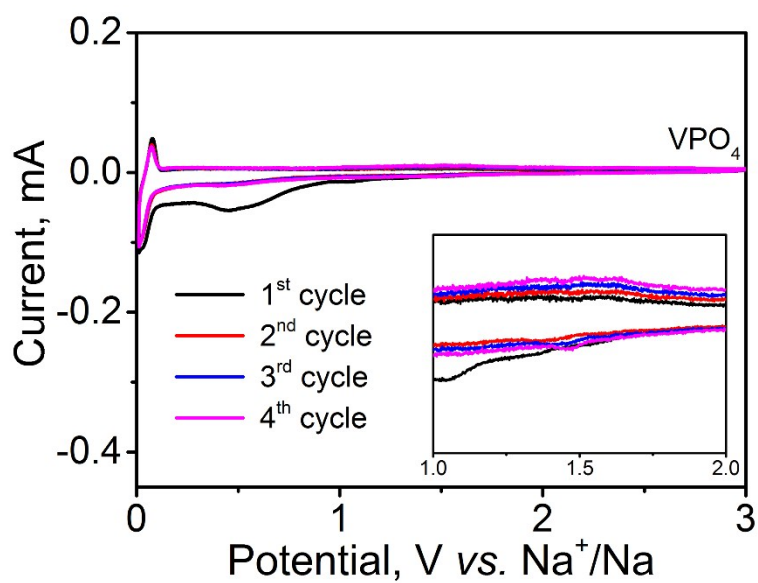


Fig. S9. The CV plots of VPO_4 in the first 4 cycles between 0.01 V and 3.0 V at a scanning rate of 0.1 mV s^{-1} .

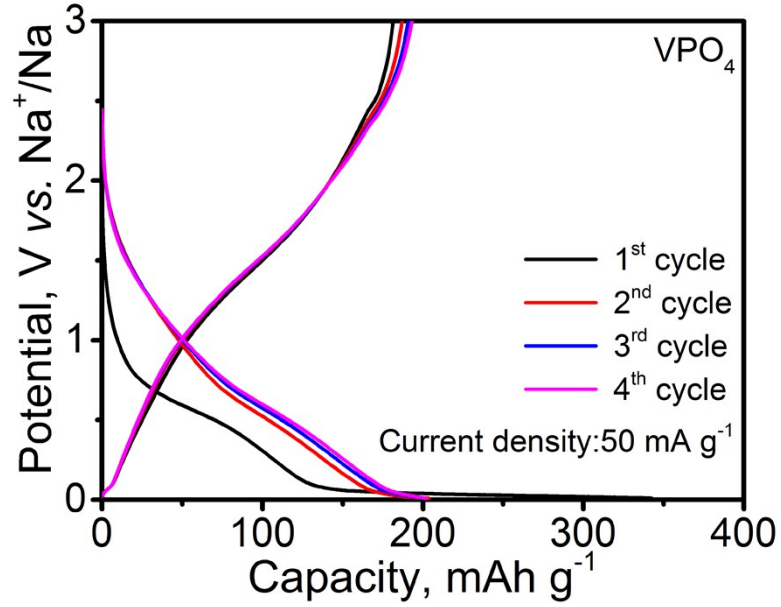


Fig. S10. The charge/discharge curves of VPO_4 in the first 4 cycles between 0.01 V and 3.0 V at rate of 50 mA g^{-1} .

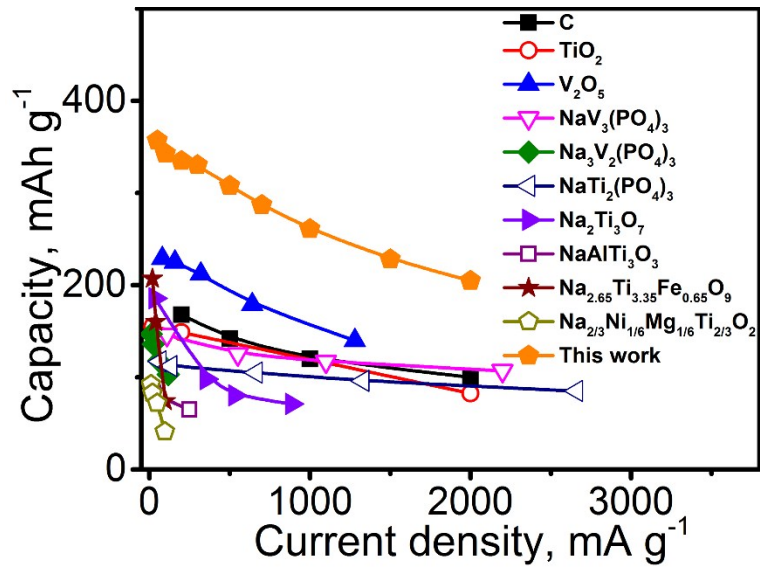


Fig. S11. Performance comparison of $\text{VPO}_4@\text{C}$ with other recently reported anodes for SIBs

Table S4. Comparison of electrochemical performance for VPO₄@C with other materials reported elsewhere as the anode materials for SIBs.

Sample	Rate capability Capacity/current (mAh g ⁻¹ /mA g ⁻¹)	Cycling stability Capacity/current/cycles (mAh g ⁻¹ /mA g ⁻¹ /n)	Reference s
VPO ₄ @C	204.8/2000	245.3/1000/200	This work
C	100/2000	160/100/100	S5
TiO ₂	82.7/2000	160/20/50	S6
V ₂ O ₅	140/1280	177/40/100	S7
NaV ₃ (PO ₄) ₃	107/2200	126/220/100	S8
Na ₃ V ₂ (PO ₄) ₃	103/117	136/12/50	S9
NaTi ₂ (PO ₄) ₃	85/2660	77/1330/1000	S10
Na ₂ Ti ₃ O ₇	71/885	125/35.4/50	S11
NaAlTi ₃ O ₃	65/250	62/25/100	S12
Na _{2.65} Ti _{3.35} Fe _{0.65} O ₉	74.2/100	110/40/100	S13
Na _{2/3} Ni _{1/6} Mg _{1/6} Ti _{2/3} O ₂	41/96	80.4/9.6/100	S14

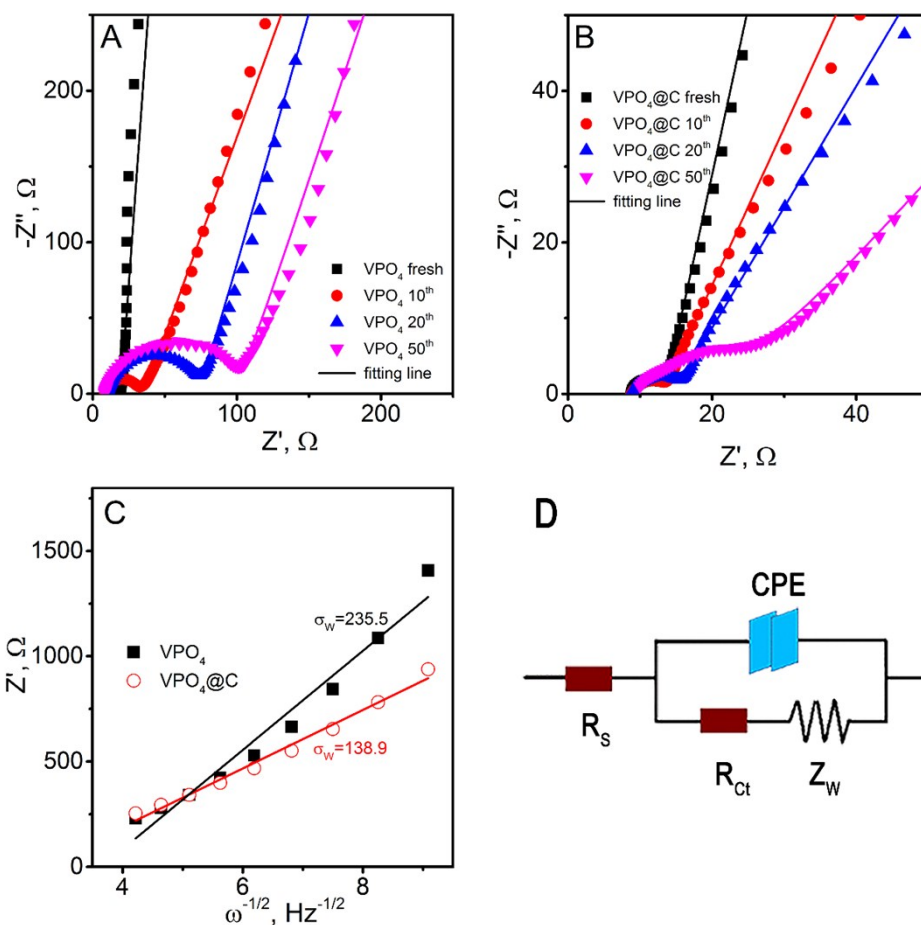


Fig. S12. The recorded impedance spectra of VPO₄ (A) and VPO₄@C (B) before and after various cycles, linear fitting to Z' versus $\omega^{-1/2}$ plots in the low-frequency range (C), equivalent circuit used for fitting the experimental EIS data (D).

Table S5. Result of electrochemical impedance and Warburg coefficient in Figure S13.

Samples	Cycle number, n	R_s, Ω	R_{ct}, Ω	$\sigma_w, \Omega s^{-1}$	$D_{Na}, cm^2 s^{-1}$
VPO ₄	Pristine	13.01	4.26	235.5	8.19×10^{-15}
	10	14.83	19.15		
	20	14.98	64.52		
	50	14.68	93.25		
VPO ₄ @C	Pristine	8.61	2.58	138.9	2.35×10^{-14}
	10	8.97	4.15		
	20	8.84	5.46		
	50	9.32	14.17		

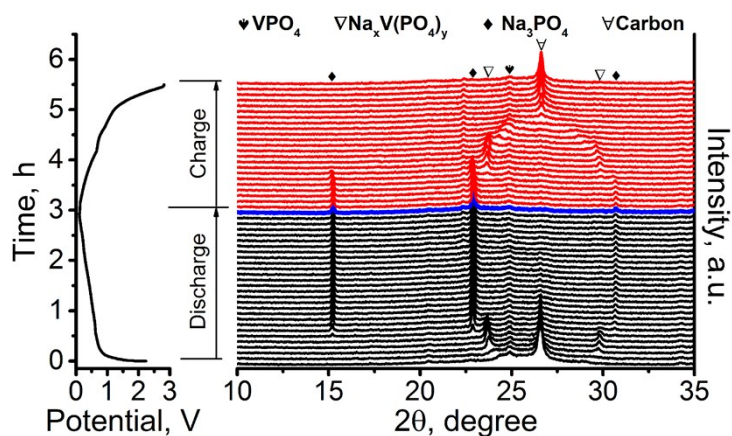


Fig. S13. Selected 2θ regions plot of *in-situ* XRD results of VPO_4/C electrode against the voltage profile during the initial cycle.

For *in-situ* XRD measurement, the cell was galvanostatic charged/discharged at a current rate of 100 mA g^{-1} , while each XRD patterns were collected at different desodiation/sodiation state in the first cycle and stacked together sequently. Meanwhile, the corresponding contour plot of *in-situ* patterns is displayed in Fig. 4A. The phase compositions are color-coded to have a better distinction for desodiation/sodiation process. The red color means low intensity, and the blue color means high intensity, which are shown in the right side of Fig. 4A. It is better to observe the phase transformation by combination of charge/discharge curves and XRD pattern at various desodiation/sodiation states.

The intermediate phase is a new material with peaks located at 2θ of 24° and 30.5° , which are neither Na_3PO_4 nor VPO_4 , probably ascribed to the combination of Na^+ and VPO_4 and formation of $\text{Na}_x\text{V}(\text{PO}_4)_y$. The $\text{Na}_x\text{V}(\text{PO}_4)_y$ could be indexed into the $\text{Na}_3\text{V}_3(\text{PO}_4)_3$ or $\text{Na}_4\text{V}_2(\text{PO}_4)_3$, which can be found in the other polyanion anode materials of sodiated $\text{NaV}_3(\text{PO}_4)_3$ ^{S15,S16} and $\text{Na}_3\text{V}_2(\text{PO}_4)_3$ ^{S17,S18} respectively. However, the intermediate $\text{Na}_x\text{V}(\text{PO}_4)_y$ is metastable and hardly to determine the accurate

structure, and this phenomenon usually occurs in the halfway of sodiation/desodiation process.^{S15-S18} Under the limit of experiment condition, other characterizations should be carried out to verify the intermediate phase.

Reference

- S1. X. Ou, X. Xiong, F. Zheng, C. Yang, Z. Lin, R. Hu, C. Jin, Y. Chen and M. Liu, *J. Power Sources*, 2016, **325**, 410.
- S2. C. Yang, X. Ou, X. Xiong, F. Zheng, R. Hu, Y. Chen, M. Liu and K. Huang, *Energy Environ. Sci.*, 2017, **10**, 107.
- S3. K. Cui, S. Hu and Y. Li, *Electrochim. Acta*, 2016, **210**, 45.
- S4. Z. Huang, H. Hou, C. Wang, S. Li, Y. Zhang and X. Ji, *Chem. Mater.*, 2017, **29**, 7313
- S5. K. Tang, L. Fu, R. J. White, L. Yu, M.-M. Titirici, M. Antonietti and J. Maier, *Adv. Energy Mater.*, 2012, **2**, 873.
- S6. S. M. Oh, J. Y. Hwang, C. S. Yoon, J. Lu, K. Amine, I. Belharouak and Y. K. Sun, *ACS Appl. Mater. Interfaces*, 2014, **6**, 11295.
- S7. D. Su, S. Dou and G. Wang, *ChemSusChem*, 2015, **8**, 2877.
- S8. P. Hu, X. Wang, J. Ma, Z. Zhang, J. He, X. Wang, S. Shi, G. Cui and L. Chen, *Nano Energy*, 2016, **26**, 382.
- S9. Z. Jian, Y. Sun and X. Ji, *Chem. Commun.*, 2015, **51**, 6381.
- S10. C. Wu, P. Kopold, Y.-L. Ding, P. A. van Aken, J. Maier and Y. Yu, *ACS Nano*, 2015, **9**, 6610.
- S11. A. Rudola, K. Saravanan, C. W. Mason and P. Balaya, *J. Mater. Chem. A*, 2013, **1**, 2653.
- S12. X. Ma, K. An, J. Bai and H. Chen, *Sci. Rep.*, 2017, **7**, 162.
- S13. M. Xu, J. K. Hou, Y. B. Niu, G. N. Li, Y. T. Li and C. M. Li, *Chem. Commun.*, 2015, **51**, 3227.
- S14. P. F. Wang, H. R. Yao, T. T. Zuo, Y. X. Yin and Y. G. Guo, *Chem. Commun.*, 2017, **53**, 1957.
- S15. X. Wang, P. Hu, P. Hu, L. Chen, Y. Yao, Q. Kong, G. Cui, S. Shi and L. Chen, *J. Mater. Chem. A*, 2017, **5**, 3839.
- S16. P. Hu, X. Wang, J. Ma, Z. Zhang, J. He, X. Wang, S. Shi, G. Cui and L. Chen, *Nano Energy*, 2016, **26**, 382.
- S17. D. Wang, N. Chen, M. Li, C. Wang, H. Ehrenberg, X. Bie, Y. Wei, G. Chen and F. Du, *J. Mater. Chem. A*, 2015, **3**, 8636.
- S18. Z. Jian, Y. Sun and X. Ji, *Chem. Commun.*, 2015, **51**, 6381.